High Efficiency and Stable Perovskite Solar Cell Using ZnO/rGO QDs as an Electron Transfer Layer

Mohammad Mahdi Tavakoli, Rouhollah Tavakoli, Zahra Nourbakhsh, Aashir Waleed, Umar Siddique Virk, and Zhiyong Fan**

Fabrication of organohalide perovskite materials on the top of ZnO nanoparticles (NPs) has some beneficial advantages such as room temperature processing; however, the perovskite is not stable on ZnO NPs layer during the annealing process. In fact, there are only a few reports about the fabrication of perovskite solar cells on ZnO NPs layer. Herein, the decomposition mechanism of $CH_3NH_3PbI_3$ perovskite materials on ZnO is reported, and it is found that the perovskite film on the top of the ZnO layer is converted into PbI_2 during the annealing process due to the existence of hydroxide groups on the surface of the ZnO NPs. Depending on the annealing temperature, the reaction rate and the quality of the perovskite film can be changed. In order to tackle this problem, a quasi core shell structure of ZnO/reduced graphene oxide (rGO) quantum dots is synthesized and is employed as an electron transfer layer. In this regard, rGO not only passivates the surface of the ZnO NPs to prevent the reaction, but also extracts the charge carriers quickly from the perovskite layer to reduce the carrier recombination. Our results show that perovskite solar cell on ZnO/rGO layer exhibits a stable power conversion efficiency as high as 15.2% and 11.2% on fluorine-doped tin oxide (FTO) glass and polyethylene terephthalate (PET) substrates, respectively, under AM1.5G illumination.

1. Introduction

Recently, solid-state organic–inorganic lead halide perovskite materials with a rapid progress have attracted tremendous attention because of their long diffusion length up to 175 µm,[1,2] high carrier mobility, direct optical bandgap, broad absorption range, low-cost processing, and ease of fabrication.[3–5] These features make them exceptional choices for fabrication of high efficiency photovoltaic (PV) devices. To date, a power conversion efficiency (PCE) more than 20% has been achieved using a solution process.[6–10] Among the different processes for fabrication of perovskite solar cells, including one-step solution process,[11,12] sequential deposition,[13,14] vacuum deposition,[15] and chemical vapor deposition,[16] a two-step solution process has benefits such as good control of the crystal structure for perovskite film.[17]

In order to fabricate perovskite solar cells, different types of electron transfer layers (ETLs) and hole transfer layers (HTLs) have been employed. Among them, a conducting polymer such as poly(3,4-ethylenedioxythiophene):polystyrenesulfonate (PEDOT:PSS) is commonly used as the HTL in perovskite solar cells. However, the high acidity of this polymer deteriorates the ITO layer, and its high hygroscopicity can also accelerate degradation of the device due to water absorption.[18] Recently, many research groups have focused on inorganic materials that can work as an HTL, such as CuSCN and NiO.[19–21] Regarding the ETL materials, more stable metal oxides, such as titanium dioxide (TiO_2), zinc oxide (ZnO), and tin oxide (SnO_2) have been developed for perovskite solar cells.[22] Among these metal oxides, TiO_2-nanoparticles (NPs) have been commonly used as the ETL to provide an efficient charge collection.[23] In order to prepare a TiO_2 mesoporous layer, a sintering process with high temperature (≈500 °C) is required.[18] This temperature is too high for fabrication of perovskite on plastic substrate. In addition, few groups already have reported ETL-free perovskite solar cell with descent PCE on plastic substrates; however, their PCE is not comparable with those devices fabricated on rigid substrates.

ZnO NPs are, therefore, a promising candidate to replace TiO_2 NPs as the ETL layer in perovskite solar cells. However, only a few works have reported perovskite solar cells based on ZnO NPs. Intriguingly, the devices on ZnO NPs show a maximum PCE of close to 15.7%,[24] which is lower than those on TiO_2 NPs. To fabricate the device on ZnO NPs, a two-step solution process is usually employed. Depending on the annealing temperature (70 °C–100 °C) of the perovskite film, different works have reported a device performance from 8.9% to 15.7%.[24–27] In addition, a few works have demonstrated the instability of perovskite materials on top of ZnO NPs due to

Dr. M. M. Tavakoli, A. Waleed, U. S. Virk, Prof. Z. Fan
Department of Electronic and Computer Engineering
Hong Kong University of Science and Technology
Clear Water Bay, Kowloon, Hong Kong
E-mail: mmtavakoli@ust.hk; eezfan@ust.hk
Dr. M. M. Tavakoli, Prof. R. Tavakoli, Z. Nourbakhsh
Department of Materials Science and Engineering
Sharif University of Technology
Tehran, Iran, P.O. Box 11365-9466
A. Waleed
Electrical, Electronics and Telecommunication Engineering Department
University of Engineering and Technology Lahore
Lahore, Pakistan, P.O. Box 54890

DOI: 10.1002/admi.201500790

the deprotonation of the methylammonium cation in the presence of hydroxide groups at the surface of ZnO NPs.[28] These works mentioned that the annealing temperature and time are two key parameters to fabricate an efficient and stable device on ZnO NPs.

Recently, a monolayer of graphene with a honeycomb lattice and its hybrid materials with different NPs have attracted considerable attention for use in photovoltaic applications due to the fact that they work as a fast electron funnel.[29,30] In these hybrid nanostructures, graphene is an efficient and fast charge extraction layer.[31–33] In our previous works, we fabricated hybrid nanostructures of PbS quantum dots (QDs) and graphene and employed them as an absorber layer in quantum dot solar cells and improved the performance of the device by up to 40%.[34–38] Wang et al.[39] also demonstrated that the hybrid nanostructure of graphene and TiO_2 NPs can improve the device performance of a perovskite solar cell up to 15.6%. They used graphene nanoflakes to enhance the charge-collection of electrons, resulting in higher efficiency.

In this work, we systematically investigated the instability issue of $CH_3NH_3PbI_3$ perovskite material on top of ZnO NPs. Our results show that the perovskite film decomposes and is converted into PbI_2 film during the annealing process at 100 °C. X-ray photoelectron spectroscopy (XPS) analysis illustrates the presence of hydroxide groups on the surface of the ZnO NPs, and they induce decomposition of perovskite material due to the deportation of the methylammonium cation. To tackle this problem, we synthesize a quasi-core–shell structure of ZnO/rGO QDs and employ it as an ETL in a perovskite solar cell. The results of PV measurements and characterization tests demonstrate that the $CH_3NH_3PbI_3$ perovskite material demonstrate excellent stability on top of the ZnO/rGO QDs layer after the annealing process at 100 °C due to the lower amount of hydroxide groups after surface modification of ZnO with rGO. In addition, the results of external quantum efficiency (EQE), time-resolved photoluminescence (TRPL), and electrochemical impedance spectroscopy (EIS) measurements show the enhancement of current density and device performance using the ZnO/rGO QDs layer. Finally, power conversion efficiencies (PCE) of 15.2% and 11.2% are achieved on FTO glass and polyethylene terephthalate (PET) substrates, respectively, under AM 1.5G illumination.

2. Results and Discussion

2.1. Instability of $CH_3NH_3PbI_3$ Perovskite Material on ZnO NPs

In order to fabricate the perovskite solar cell on ZnO NPs film, ZnO NPs with an average size of 3 nm (Figure S1, Supporting Information) are synthesized by a solution process, as reported elsewhere.[24] Then, a $CH_3NH_3PbI_3$ perovskite layer is deposited on the ZnO NPs film using a two-step solution process. The photovoltaic devices have a general structure of FTO/ZnO/$CH_3NH_3PbI_3$/spiro-OMeTAD/Au. The details of the fabrication process are mentioned in the experimental section.

Up to now, a few works have reported that the perovskite is not stable on top of the ZnO layer after annealing at 100 °C, especially using a one-step process.[28] While Liu et al.[24] showed a highly efficient perovskite solar cell on ZnO NPs, close to 16%, without annealing, other researchers have demonstrated that the annealing of the perovskite at lower temperature results in poor device performance.[18] In our work, we fabricate the perovskite solar cells on ZnO NPs without annealing and with an annealing process at 70 °C and 100 °C. The inset images in **Figure 1**a_1–a_3 show the photographs of the samples. Without annealing the color is brownish with a small grain size, as shown in Figure 1a_3, but after annealing at 100 °C the perovskite film is converted into a yellowish film, i.e., a PbI_2 layer (Figure 1a_1). According to Figure 1a_2 and its inset image, it seems that perovskite material does not react with the ZnO NPs layer at 70 °C. However, the sample is brownish, which may be because there is still a local reaction at the interfacial regions between the perovskite and ZnO NPs film.

The results of the *J*–*V* measurements for the perovskite solar cells on ZnO NPs are presented in Figure 1b and **Table 1** under AM 1.5G illustration at 1 sun. As can be seen, without annealing the result is an open-circuit voltage (V_{oc}) of 0.8 V, short- circuit current density (J_{sc}) of 9.5 mA cm^{-2}, and fill factor (FF) of 48%, resulting in a PCE of 3.6%. We have found that the small grain size in the perovskite film (Figure 1a_3) may be the main reason for the poor PCE due to a high recombination rate at grain boundaries. The device performance after annealing the perovskite film on the ZnO NPs layer at 100 °C is only 1.1% due to the reaction between the perovskite film and ZnO NPs. Thus, we have decreased the annealing temperature to 70 °C and we have not observed any reaction on the perovskite film after annealing (Figure 1a_2), however, there may still be a reaction at the interfacial region. Finally, a PCE of 7.5% is attained from this sample. The EQE spectrum and the calculated current density of perovskite solar cells on ZnO layer at different annealing temperature are shown in Figure S2 (Supporting Information).

To study the surface of the ZnO film, X-ray photoelectron spectroscopy (XPS) is employed. The deconvolution of the O 1s XPS core-level spectrum of ZnO is shown in Figure 1c. As can be seen, the O 1s peak can be deconvoluted into two main peaks located at 530 and 531.9 eV, which are related to the O 1s level and chemisorbed agents such as hydroxide (OH^-) in the ZnO film, respectively. As a result, the ZnO NPs have some oxygen agents, such as hydroxide, on their surface that could decompose the $CH_3NH_3PbI_3$ perovskite material. In this regard, methylammonium iodide (MAI) absorbs hydroxide groups and is converted to CH_3NH_3OH, and during annealing, this product is decomposed to CH_3NH_2 and H_2O in the gaseous phase.[18] Such reactions could be the main reason for the decomposition of the perovskite film into the PbI_2 layer. Furthermore, the results of X-ray diffraction (XRD) of the perovskite film under the different post-treatment conditions have good agreement with our discussion (Figure S3, Supporting Information). The results show that the peaks located at 14.1° (110), 28.4° (220), and 42.1° (330) have the highest intensity after annealing at 70 °C. Also, without annealing, the peaks intensity is very low. Meanwhile, by increasing the annealing temperature to 100 °C, the intensity of the peak at 12.7°, which is for PbI_2, is significantly increased. This depicts that the perovskite materials on the ZnO NPs layer completely converted into PbI_2 film after the annealing process at 100 °C for 30 min. Furthermore, the PbI_2

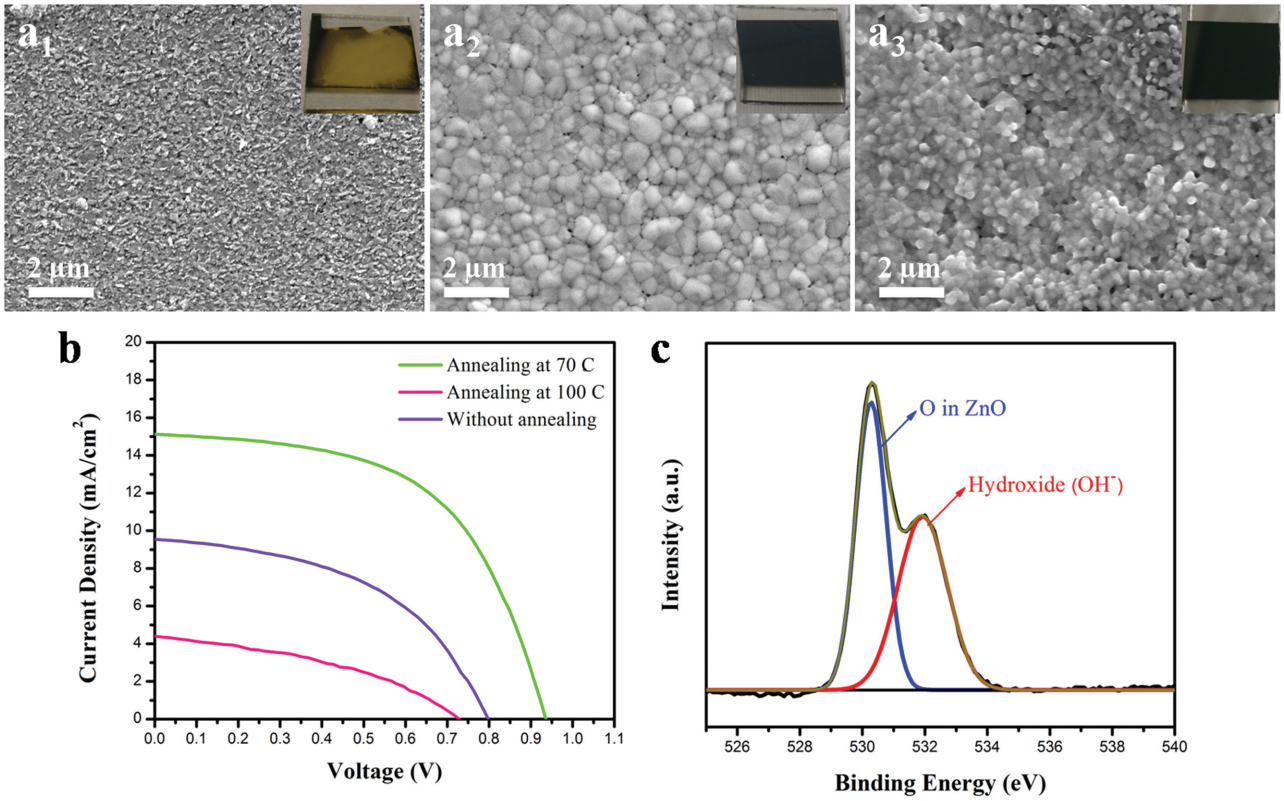

Figure 1. The top-view SEM images of $CH_3NH_3PbI_3$ perovskite on top of ZnO film after annealing for 30 min at a_1) 100 °C, a_2) 70 °C, and a_3) without annealing. The inset images are the photographs of the samples after the annealing process. b) Current density–voltage (*J*–*V*) measurement of the perovskite solar cells on ZnO film for different annealing conditions. c) High-resolution of O 1s XPS core-level spectrum of ZnO.

peak in the perovskite film after annealing at 70 °C indicates that there is still a reaction at the interfacial region of the perovskite and ZnO NPs films.

2.2. Characterization of ZnO/rGO QDs

To solve the instability problem of the perovskite film on top of the ZnO NPs, we fabricate a quasi-core–shell structure of ZnO/rGO QDs using a facile solution process as mentioned in the experimental section. In fact, the rGO shell works as a protection layer for ZnO NPs to prevent the reaction. Equation (1) shows the synthesis process of the ZnO NPs in DMF:

$$\mathrm{Zn(CH_3COO)_2\,CH_2O + (CH_3)_2\,NC(O)H} \rightarrow \mathrm{ZnO + (CH_3COO)_2\,CHN(CH_3)_2 + H_2O} \quad (1)$$

Table 1. Figure of merits for the perovskite device on ZnO film with different annealing conditions (each number is the average of 10 devices).

Device	V_{oc} [V]	J_{sc} [mA cm^{-2}]	Fill factor [%]	PCE [%]
Device without annealing	0.8 ± 0.04	9.5 ± 1.2	48 ± 3	3.6 ± 0.7
Annealed at 100 °C	0.73 ± 0.05	4.4 ± 1.5	34 ± 5	1.1 ± 0.5
Annealed at 70 °C	0.94 ± 0.03	15.1 ± 1.3	53 ± 2	7.5 ± 0.3

By adding the GO nanosheets to the above reaction, two mechanisms can be enabled:

1) the formation of Zn—O—C bonds after chemisorption of Zn^{2+} ions on the surface of the embryonic ZnO QDs and reaction with GO functional groups, and 2) the reaction of Zn^{2+} ions with GO to establish Zn—O bonds and combine with embryonic ZnO QDs. The layer-by-layer chemical exfoliation process of GO nanosheets occurs during these reactions and ZnO QDs are wrapped with rGO as a hybrid structure.[33,35,40]

Figure 2a shows the TEM images of ultrafine ZnO/rGO QDs with an average size of about 5 nm (Figure S5, Supporting Information). As can be observed, ZnO/rGO QDs have a core–shell structure. The TEM image illustrates that the ZnO core has an interplanar spacing of 0.26 nm, which corresponds to the distance between two (002) planes in the hexagonal structure of zinc oxide with the [002] growth direction (c axes).[40] The rGO shell has an interplanar spacing of 0.14 nm, matching with the hexagonal atomic lattice of graphene.[35] Figure 2b shows the EDS mapping analysis of the ZnO/rGO QDs taken from area A (Figure 2a). As can be seen, there is not a carbon grid in this area and as a result, the carbon signal is corresponded to the graphane nanoshell covering the surface of the ZnO QD. In addition, Figure 2c,d show the XRD pattern and Raman spectrum of the ZnO/rGO QDs, where the diffraction peaks of the ZnO/rGO QDs are related to the crystalline ZnO (JCPDS no. 36-1451), and the ultrathin rGO layers (2θ = 25.81, 43.51) support the formation of the hybrid

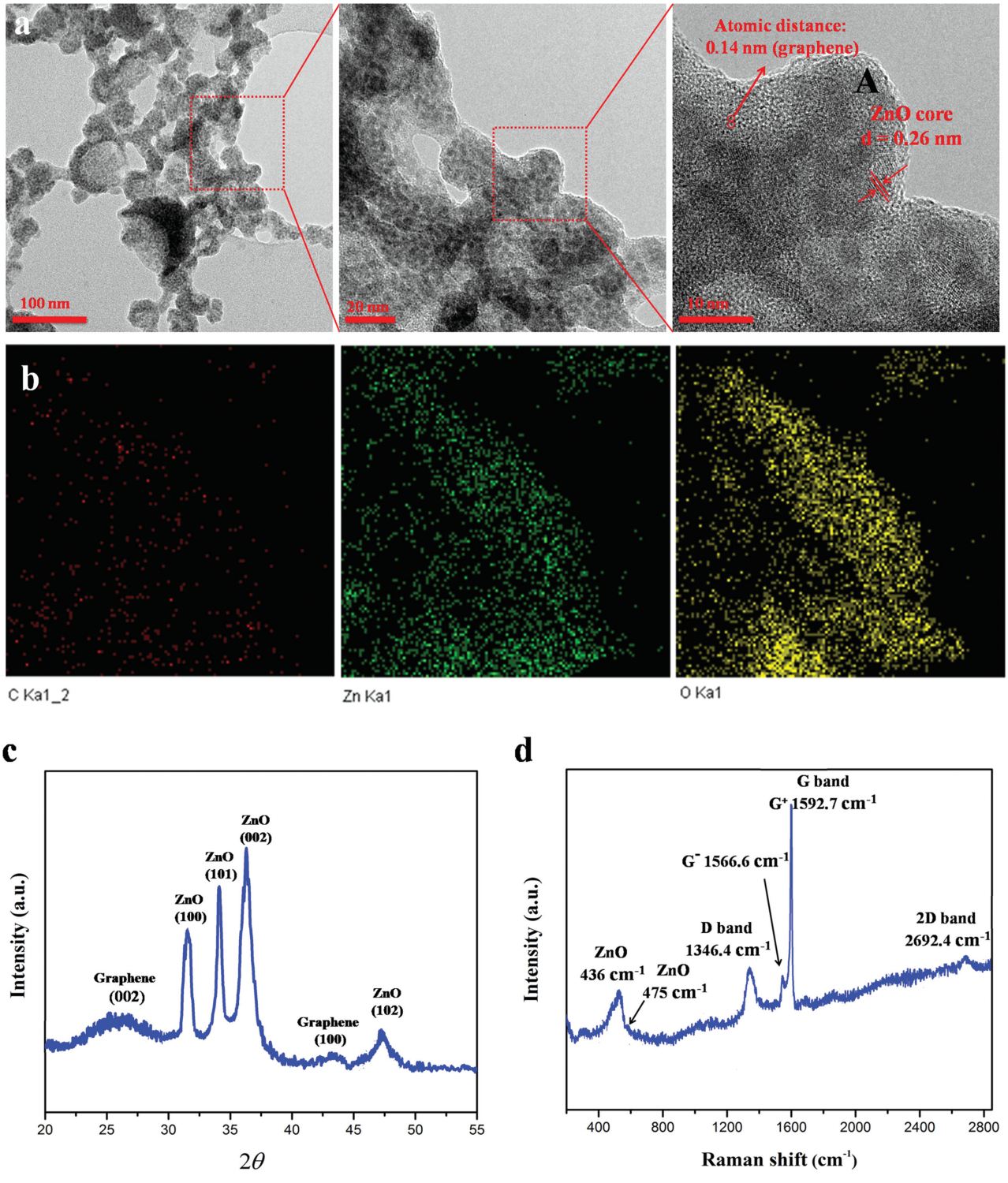

Figure 2. a) TEM images of ZnO/rGO QDs with different magnification. b) The EDS mapping of the selected area (A) for Zn, O, and C. c) XRD pattern and d) Raman spectrum of the ZnO/rGO QDs film.

structure.[33,35] The Raman peaks also demonstrate the presence of rGO at the surface of the ZnO core. Moreover, the splitting of the G peak into two sub-bands, namely G^+ (1592.7 cm^{-1}) and G^- (1566.6 cm^{-1}) is due to the induced strain by wrapping the rGO shell around the ZnO core.[20] As a result, at the surface of the ZnO core, Zn^{2+} ions react with the GO functional groups to form local Zn—O—C bonds and chemical exfoliation of GO occurs.[33] In addition, the presence of a D-band at 1346.4 cm^{-1} depicts the existence of defects and strain in the graphitic sheets due to their bending. Moreover, the position of a 2D

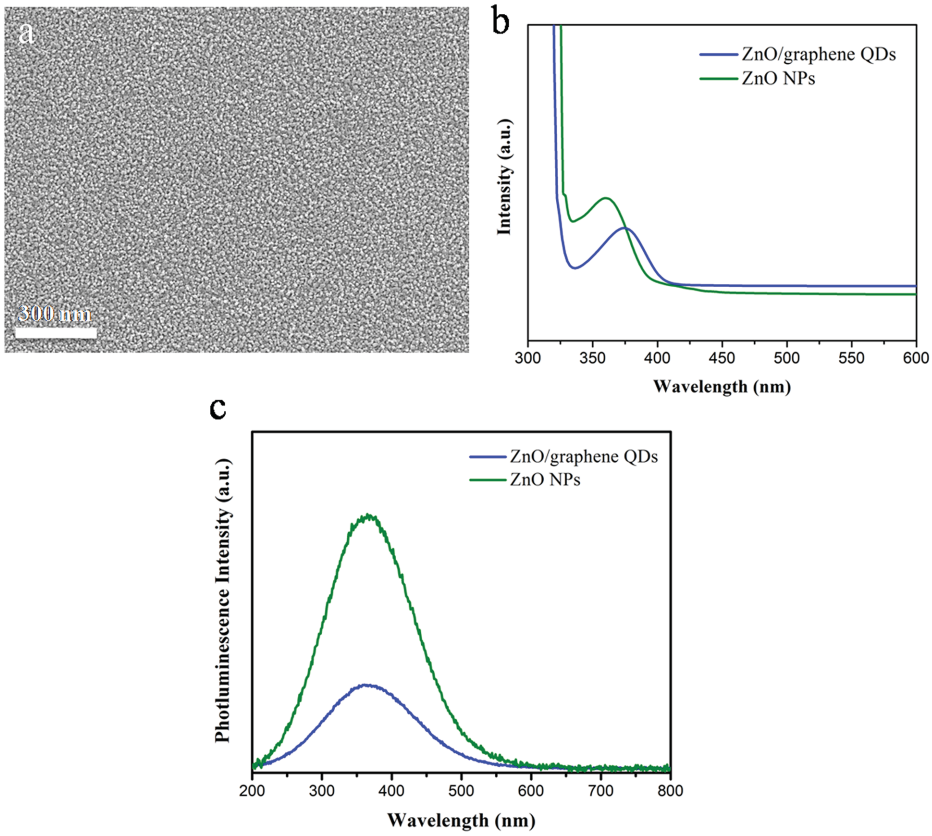

Figure 3. a) The top-view SEM image of ZnO/rGO QDs deposited by electrophoretic method. b) The absorption, and c) PL spectra of ZnO NPs and ZnO/graphene QDs.

peak at 2692.4 cm^{-1} could support the formation of an ultrathin rGO shell upon chemical processing.[40] The EDS analysis and XPS pattern of ZnO/rGO QDs support the composition of this material, as shown in Figure S4 (Supporting Information). The XPS results indicate the bonding energies of different components for emitted electrons at 1022.38 (Zn2p3/2), 531.8 (O1s), and 284.6 eV (C1s). The strong C1s and O1s peaks correspond to the carbon element in association with oxygen in GO and lattice oxygen in ZnO, respectively.[40] In addition, the high-resolution of O 1s XPS core-level spectrum of ZnO/rGO thin film (Figure S6, Supporting Information) demonstrates that the intensity of hydroxide group is drastically decreased after surface modification ZnO QDs by rGO, resulting in lower possibility for perovskite decomposition.

To probe the effect of ZnO/rGO QDs film as an ETL, its surface morphology and optical properties are studied. **Figure 3**a depicts the top-view SEM image of this layer with a high coverage and uniformity. Ultraviolent-visible (UV–vis) spectroscopy of ZnO/rGO QDs as compared to ZnO NPs shows an auxiliary enhanced absorption edge to longer wavelengths (a red shift of ≈25 nm) because of their larger size, as shown in Figure 3b. The photoluminescence (PL) measurement (Figure 3c) also demonstrates a luminescence quenching effect of the rGO shell by about 72% as compared to the ZnO NPs film. Moreover, the transmittance and surface roughness of ZnO/rGO film using atomic force microscopy (AFM) are investigated, as shown in Figure S7 (Supporting Information). The optimum transmittance of the ZnO/rGO film is around 80% which is suitable for device fabrication. The AFM image of film indicates a very fine and uniform layer of ZnO/rGO, as illustrated in Figure S7b (Supporting Information). Also, the surface roughness of film is ≈9.7 nm.

2.3. Fabrication of Perovskite Solar Cell on ZnO/rGO Electrode

Figure 4a illustrates a cross-sectional SEM image of the perovskite solar cell on a ZnO/rGO QDs electrode, which was deposited on FTO glass using the electrophoretic method. The perovskite film is fabricated on the electrode by a two-step solution process. First, a PbI_2 layer is spin-coated on the ZnO/rGO electrode (≈50 nm) and after drying, the chip is immersed into the MAI solution in order to synthesize the $CH_3NH_3PbI_3$ perovskite film (≈300 nm) followed by annealing at 100 °C for 30 min. Thereafter, 2,2′,7,7-tetrakis(*N*,*N*-di-p-methoxyphenylamine)-9,9-spirobifluorene (Spiro-OMeTAD) as an HTL is spin coated on the perovskite film, and finally, 100 nm of gold is thermally evaporated on a Spiro-OMeTAD to complete the device structure, as schematically shown in Figure 4b.

The crystal structure of the perovskite layer and its absorbance are shown in Figure 4c,d, respectively. As can be seen, the average grain size of the perovskite material on the ZnO/rGO

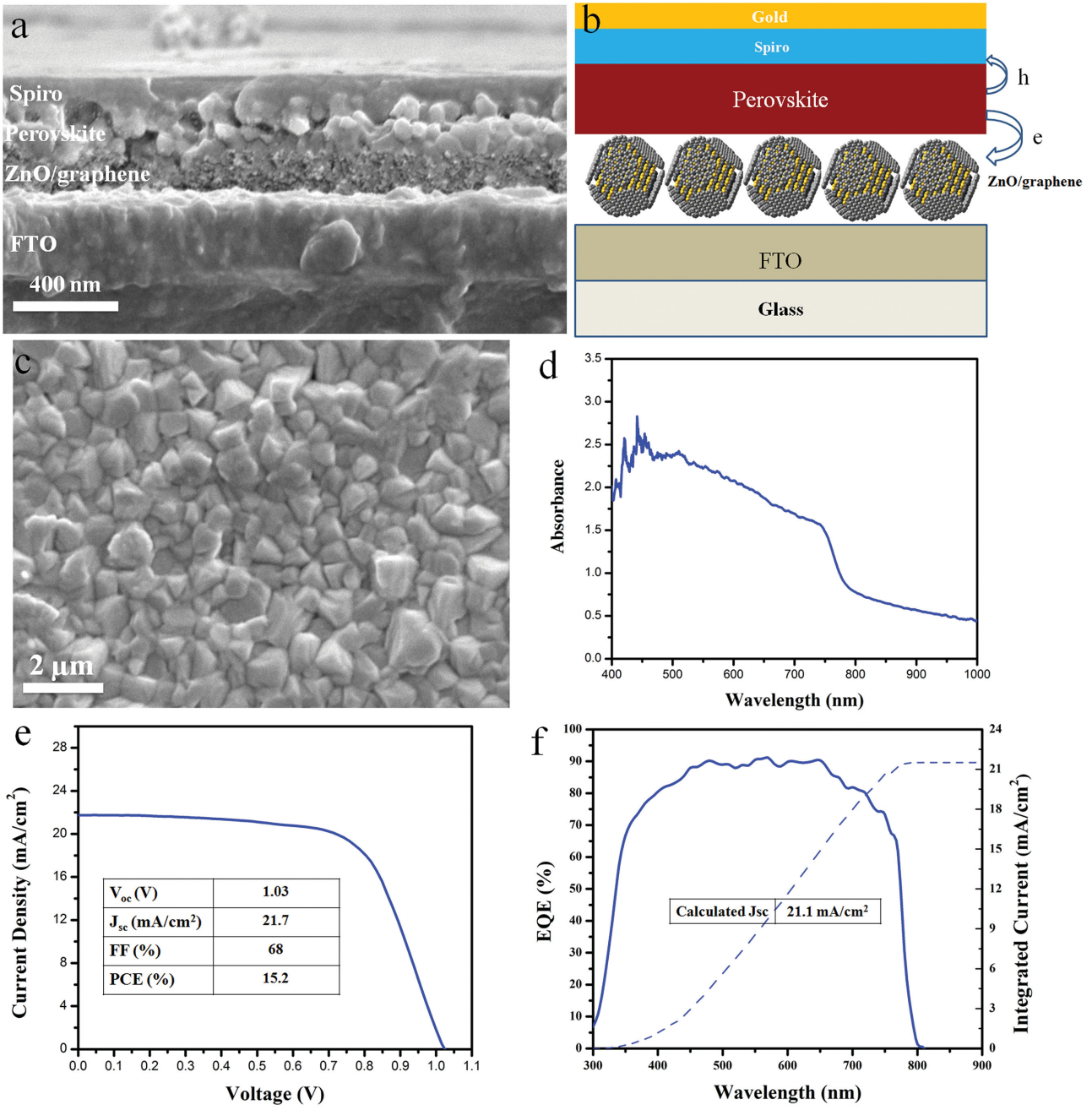

Figure 4. a) The cross-sectional SEM and b) schematic images of perovskite solar cell on ZnO/rGO film. c) Top-view SEM image, and d) the absorbance spectrum of perovskite film on top of ZnO/rGO electrode. e) *J–V* measurement, and f) EQE spectrum of champion perovskite solar cell device based on ZnO/rGO electrode.

electrode is more than 1µm, which is larger than that of the perovskite on the ZnO layer due to the higher annealing temperature, time, and the nature of this hybrid structure as a porous electrode. Moreover, the absorbance of the perovskite film indicates that it has a suitable bandgap of ≈1.59 eV (780 nm) for solar cell application. The XRD pattern of the perovskite film on the ZnO/rGO is demonstrated in Figure S8 (Supporting Information), and is in good agreement with the literature.[35]

The current density–voltage (*J–V*) measurement of the perovskite solar cells on the ZnO/rGO electrode is performed under simulated AM 1.5G solar irradiation in air. Figure 4e shows the performance of the $CH_3NH_3PbI_3$ perovskite solar cells. The results indicate that the maximum PCE (15.2%) belongs to the perovskite solar cell on the ZnO/rGO electrode with a thickness of 50 nm. The J_{sc} and fill factor (FF) of this device are 21.7 mA cm^{-2} and 68%, respectively. The inset table in Figure 4e summarizes the figures of merit for the champion device. In addition, by using a thicker layer of ZnO/rGO QDs film, for instance 100 nm, the PCE drops 40% due to the lower transmittance (Figure S9, Supporting Information). Note that

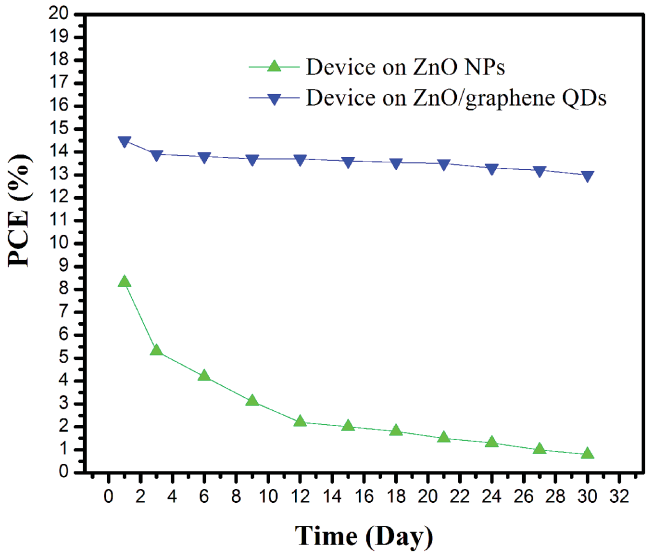

Figure 5. Stability of the devices based on ZnO NPs and ZnO/rGO QDs in an ambient environment after encapsulation using UV-epoxy.

the results of the *J*–*V* measurements obtained by the reverse scan and the forward scan are slightly different, as shown in Figure S10 (Supporting Information). To investigate the short current density of the champion device, the EQE spectrum is measured, as shown in Figure 4f. Integrating the overlap of the EQE spectrum with the AM 1.5G solar photon flux (300 to 900 nm) yields maximum current densities of 21.1 mA cm^{-2}, which is in good agreement with the *J*–*V* measurements.

In order to study the role of rGO in the device structure, we have designed a stability test using two samples based on ZnO NPs (Annealed at 70 °C) and ZnO/rGO QDs as ETL sealed by UV-epoxy. As demonstrated in **Figure 5**, the PCE of the perovskite solar cell on ZnO/rGO drops only 10% after 30 d, which is much more stable that the ZnO one (90% drop). This experiment supports the importance of rGO in order to stop the reaction between MAI and ZnO NPs.

2.4. Characterization of Perovskite Solar Cell Based on ZnO/rGO QDs Film

To study the role of rGO combined with ZnO in the ETL layer, time-resolved photoluminescence (TRPL), electrochemical impedance spectroscopy (EIS), and ultraviolet photoelectron spectroscopy (UPS) are employed. Herein, the most important role of the rGO shell is the surface passivation of the ZnO NPs to reduce the number of dangling bonds. In fact, there are many hydroxide agents at the surface of ZnO NPs which may be passivated by the rGO shell to prevent the reaction (Figure S11, Supporting Information). In this regard, the rGO shell has a beneficial effect to reduce the instability of the perovskite on top of the ZnO NPs. The TRPL results of devices based on ZnO NPs and ZnO/rGO QDs are shown in **Figure 6**a and Table S1 (Supporting Information). The lifetime of a device based on a ZnO/rGO electrode drops significantly in the presence of rGO. The quenched spectrum of the ZnO/rGO QDs is primarily caused by static quenching and charge transfer reactions. Besides dynamic quenching, static quenching occurs when the donor and acceptor materials are in the ground state, thereby improving the carrier extraction.[31–35] In addition, faster injection of electrons from the perovskite layer to the ZnO ETL is improved by the charge separation at the interface. Thus, the charge recombination is effectively decreased, resulting in a higher J_{sc} and EQE after measurement.

To further study the role of the rGO shell, electrochemical impedance spectroscopy (EIS) analysis is employed. The results of EIS tests for devices on ZnO NPs and ZnO/rGO QDs are shown in Figure 6b. As can be seen, the Nyquist curves have been plotted for these devices in dark condition (Z' vs $-Z''$), where Z' and Z'' are the real and imaginary parts of the cell impedance, respectively. The radius of the semicircle of the device with the ZnO/rGO layer is smaller than that of the device based on the ZnO NPs electrode, suggesting that the hybrid structure of rGO and ZnO decreases the charge-transfer resistance. The calculated values of the ohmic resistance and charge-transfer resistance using the inset circuit in Figure 6b are 21.3 and 327.9 Ohm, respectively, in the ZnO/rGO-based-device, which are lower than those of the corresponding conventional device, 35.4 and 546.7 Ohm, respectively. It is clear that the device with ZnO/rGO QDs exhibits the smaller charge-transfer resistance, indicating fast electron transport properties and lower carrier recombination compared to the pristine device, as witnessed by the higher J_{sc}.

In order to plot the band diagram of the ZnO/rGO QDs based device, ultraviolet photoelectron spectroscopy (UPS) is utilized to measure its Fermi and band levels, as shown in Figure 6c. For the UPS measurement, He I (21.2 eV) is utilized as a photon source. The bandgap of the ZnO/rGO QDs is calculated using the absorption spectrum through UV–vis spectroscopy (Figure 3b). The band diagram of the solar cell based on ZnO/rGO QDs is plotted using UPS and UV–vis measurements, as illustrated in Figure 6d. As seen, the ZnO/rGO QDs film matches the perovskite layer very well, and as a result, the electrons are transferred from the absorber layer into the ZnO film easily within the rGO nanoshells. It seems that the rGO shell may improve the electrical field in this region, resulting in higher electron mobility.

In the device structure, the photoelectrons flow from the rGO shell to the ZnO core due to the lower energy level of ZnO compared to rGO.[33] Moreover, the rGO nanoshell reduces the surface carriers recombination by passivation of the dangling bonds at the surface.[26,27] The results of the TRPL and EIS tests show that in the hybrid layer the electron transfer occurs much faster than the radiative and/or nonradiative decay of photoexcitations, and as a result, the charge recombination process is significantly hindered.[33,35] Due to the efficient electron transfer between the lowest unoccupied molecular orbitals of the rGO nanoshells (acceptor) and the conduction band of the ZnO QDs (donor), the excited states are deactivated and this causes high charge generation efficiency.[40] Also, rGO with high conductivity and perfect band alignment in the device structure accelerates the electron extraction and transfer in the perovskite solar cells, resulting in higher current density and performance. In addition to the perovskite solar cell on FTO glass, we fabricate the device on an ITO-coated PET substrate using a ZnO/rGO QDs layer, and we get a PCE of 11.2%, as shown in Figure S12 (Supporting Information).

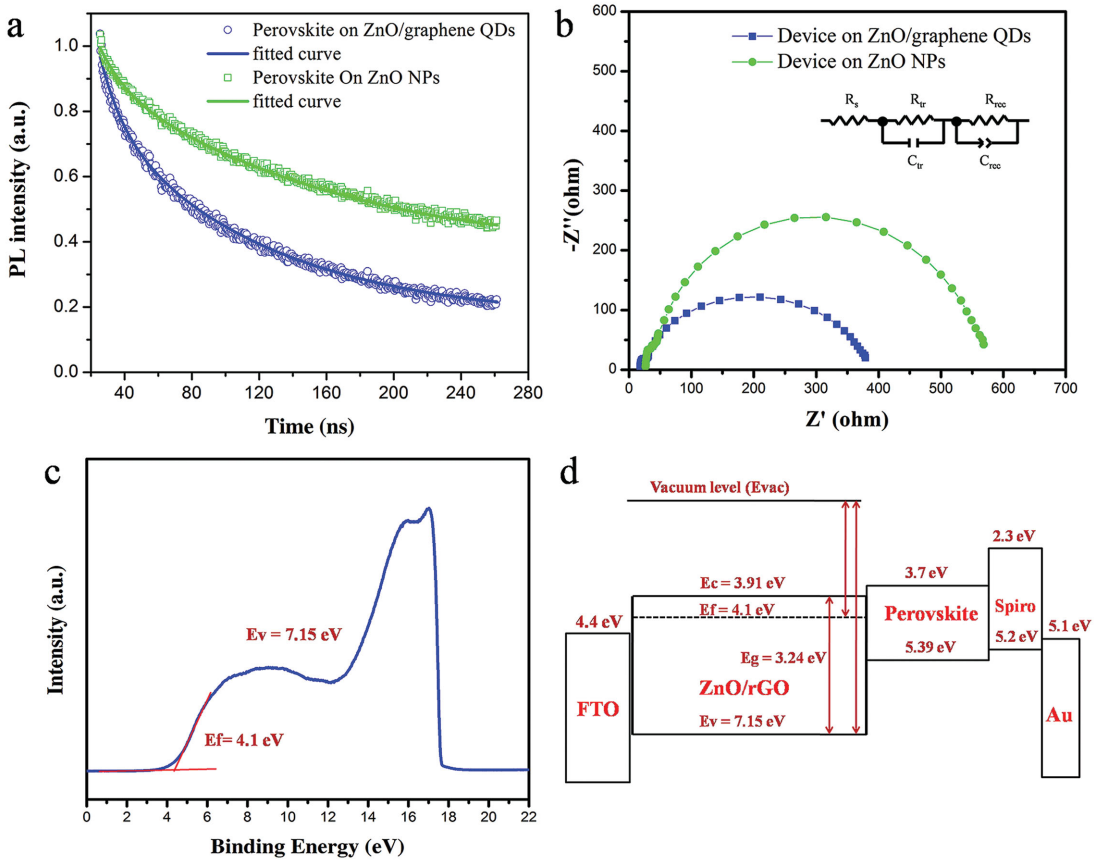

Figure 6. a) The time-resolved photoluminescence measurement and, b) electrochemical impedance spectroscopy of perovskite solar cell based on ZnO and ZnO/rGO films. c) Ultraviolet photoelectron spectroscopy of ZnO/rGO electrode. d) The schematic of band diagram of perovskite solar cell on ZnO/rGO electrode.

3. Conclusion

Herein, we investigate the reaction mechanism between ZnO NPs and MAI at different annealing temperatures and reveal that in the presence of hydroxide groups at the surface of ZnO NPs, perovskite material decomposes to PbI_2 film. To reduce the reaction rate, the annealing temperature of the perovskite film needs to be decreased to lower than 100 °C, however this compromises the crystallinity of the perovskite film. In order to tackle this problem, we demonstrate a new and simple chemical process to synthesize a quasi core–shell structure of ZnO/rGO QDs and employ it as an ETL in the perovskite solar cell. The hybrid structure has an average size of ≈5 nm, with an optical bandgap of 3.35 eV. Using this hybrid structure, $CH_3NH_3PbI_3$ perovskite material demonstrates much improved stability even with the annealing process at 100 °C. In fact, we discover that rGO works as a protection layer and improves the device stability. In addition, the ZnO/graphene layer in the device structure improves the extraction and transfer of electrons at the interface and as a result, increases the EQE and current density due to the quenching effect. This enhancement is supported by EIS, TRPL, and UPS measurements. We utilize this hybrid structure to fabricate a perovskite solar cell on FTO glass and ITO-coated PET substrates, and respectable power conversion efficiencies of 15.2% and 11.2% under AM1.5G illumination have been achieved, respectively.

4. Experimental Section

Methylammonium Iodide (MAI) Preparation: In order to synthesize MAI, 27.8 mL of methylamine (33 wt% in ethanol, Sigma-Aldrich) and 30 mL of hydroiodic acid (57 wt% in water, Sigma-Aldrich) were mixed in a 250 mL three-neck flask dropwise at 0 °C for 2 h to attain a clear solution. The solvent of this solution was evaporated using a rotary evaporator at 50 °C, and then a whitish powder (MAI) was recovered from the solution followed by purification of the MAI powder after dissolving it in absolute ethanol and precipitating it by adding diethyl ether to the solution. Finally, the MAI powder was dried at 60 °C overnight in a vacuum oven.

Synthesis of Graphene Oxide: The modified Hummers method was used to synthesize graphene oxide (GO) from graphite powder, as reported elsewhere.[35] Using this method, graphite powder (2.0 g), $NaNO_3$ (1 g), and 46 mL of H_2SO_4 were mixed at 0 °C, and then $KMnO_4$ (6 g) was added to the solution gradually during stirring for 2 h. After stirring for 30 min in a water bath (30 °C), deionized water (100 mL) was slowly added to the solution. The temperature was slowly increased to 98 °C and the mixture was maintained at this temperature for 30 min. Afterward, H_2O_2 solution (20 mL, 30%) was added to terminate the reaction, followed by adding 300 mL of deionized (DI) water (Millipore, ≈18 MΩ cm). The final color of the solution was a brilliant yellow,

indicating the oxidation of pristine graphite to GO. To remove the metal ions, the solution was then filtered and washed with diluted HCl. The pH of the product reached 7 after washing with distilled water, and finally was dried in Petri dishes at room temperature. The atomic force microscopy (AFM) image of the GO is shown in Figure S13 (Supporting Information).

Synthesis of ZnO/rGO QDs: 0.92 g zinc acetate dihydrate was dissolved in 200 mL of dimethylformamide (DMF) at room temperature. Then the GO was dissolved in DMF (1 mg mL^{-1}) and the prepared suspension was added to the zinc acetate solution dropwise during stirring at 95 °C to get a stable precursor. The solution was maintained at this temperature for 5 h until the color of the mixture changed to grayish-white. The final product was washed by ethanol and DI water several times using centrifugation and then dispersed in ethanol (24 mg mL^{-1}). Finally, ZnO QDs (without an rGO shell) were synthesized using a procedure that can be found described elsewhere.[24]

Device Fabrication: Fluorine-doped tin oxide (FTO) glass plates (Hartford Glass, USA) with an ohmic sheet resistance of 8 Ω were etched and patterned using zinc powder and HCl (2 M). The FTO glass plates were cleaned using 3 vol% Triton X-100in DI water, isopropanol, and DI water, followed by drying with a nitrogen flow. A 50 nm thick layer of ZnO or ZnO/rGO QDs was deposited on the FTO substrates by the cathodic electrophoretic deposition (EPD) technique. The EPD cell consisted of an FTO electrode and a carbon rod counter electrode positioned in parallel, at a 5 mm distance. A DC voltage of 100 V and 400 V was applied for 10 min to deposit the ZnO and ZnO/rGO layers, respectively. After washing the electrode using DI water and drying by N_2 gas, a PbI_2 solution in DMF (460 mg mL^{-1}) was then spin-coated on the electrode at 6000 rpm for 10 s and dried at 70 °C for 10 min. Then, the PbI_2-coated electrodes were immersed into a CH_3NH_3I solution (10 mg mL^{-1}) for 20 s to form the perovskite film. Afterward, the perovskite layer was annealed at 100 °C for 20 min. Subsequently, the spiro-OMeTAD (Lumtec, Taiwan) solution (80 mg mL^{-1} chlorobenzene) with 17.5 µL Li-bis(trifluoromethanesulfonyl) imide (Li-TFSI)/acetonitrile (500 mg mL^{-1}) and 28.5 µL TBP as additives was spin coated at 3000 rpm for 35 s, and the devices were left in a dry box overnight. Finally, a 100 nm Au electrode was thermally evaporated (0.08–0.12 nm s^{-1}) as an electrode. The device area was 0.15 cm^2. All of the layers were fabricated inside an Ar-filled glovebox. Oxygen and moisture levels were 7% and 20%, respectively.

Fabrication of Perovskite Solar Cell on Flexible Device: The PET/ITO substrate (South China Xiang Science & Technology Company Limited, $R \approx 8\ \Omega\ sq^{-1}$, $T \approx 78\%$) was employed to fabricate flexible device. The flexible device had a general structure of PET/ITO/ZnO-rGO/$CH_3NH_3PbI_3$/spiro-OMeTAD/Au. The fabrication process of each layer was the same as device structure on FTO glass.

Film Characterization: In order to study the thickness and morphology of the films, field-emission scanning electron microscopy (FESEM, JEOL JSM-7100F) and the X-ray diffraction method (Bruker D8 X-ray Diffractometer, USA) utilizing Cu Kα radiation were used. The optical absorption and steady-state photoluminescence spectra were measured using a Varian Carry 500 spectrometer (Varian, USA) and an Edinburgh Instruments FLS920P fluorescence spectrometer, respectively. AFM measurements of sample surfaces were acquired using a Veeco (Santa Barbara) Dimension 3100, operating in tapping mode.

Materials Characterization: The crystal structures of the materials were studied by a high-resolution transmission electron microscope (HRTEM, JOL, JEM-2100, Japan) equipped with an energy-dispersive X-ray spectrometer (EDS). Raman spectra were measured by an InVia (Renishaw AB, Sweden) spectrometer with 514.5 nm wavelength incident laser light. A hemispherical analyzer with an Al Kα X-ray source (1486.6 eV) operated at 10^{-7} Pa was used for X-ray photoelectron spectroscopy (XPS). A Varian Carry 500 spectrometer (Varian, USA) and a FLS920P fluorescence spectrometer (Edinburgh Instruments) equipped with a cryogenically cooled photomultiplier (R5509-43, Hamamatsu), with a 450 W continuous xenon arc lamp as the excitation source for steady-state spectra were employed to do the optical studies (absorption and photoluminescence (PL) spectra). A stretched exponential function $I(t) = I_0 e^{-(t/\tau)\beta}$, where τ and β are the decay time and stretch parameter, respectively, was used to fit into the PL decay curves. The spontaneous emission from a steady-state 500 mW/685 nm DPSS laser was employed as an excitation source for the measurements. The work function and valence band of the semiconducting ZnO/G layer were studied by ultraviolet photoelectron spectroscopy (UPS, AXIS NOVA, Kratos Analytical Ltd, UK) using He I (21.2 eV) as the photon source.

Device Measurements: For *J–V* measurement a solar spectrum at AM 1.5G with an intensity of 100 mW cm^{-2} was employed, including a Xe lamp and filters. The current–voltage (*J–V*) data were recorded using a Keithley 2400 (USA) instrument. The ranges of the *J–V* sweeps, scan rate, and delay time were between −1 and +1 V, 100 mV s^{-1}, and 100 ms, respectively. The devices were measured with an accuracy of ±5%. Each reported PCE was the averaged values of 10 devices ($n = 10$). A constant white light bias of ≈5 mW cm^{-2} supplied by an array of white light-emitting diodes was used to measure the EQEs as functions of the wavelength. The excitation beam coming from a 300 W xenon lamp (ILC Technology, Inc., USA) was focused through a Gemini-180 double monochromator (HORIBA Jobin Yvon IBH Ltd., Japan) and chopped at approximately 2 Hz. A Model SR830 DSP Lock-In Amplifier was used to record the signal. An Autolab PGSTAT30 (EcoChemie B.V., Utrecht, Netherlands) with a frequency range from 1 MHz down to 0.1 Hz at bias potentials 0.6 V (with a 10 mV sinusoidal AC perturbation) was employed for electrochemical impedance spectroscopy at room temperature in dark condition.

Supporting Information

Supporting Information is available from the Wiley Online Library or from the author.

Acknowledgements

This work was supported by the General Research Fund (project 612113) from the Hong Kong Research Grant Council, the Hong Kong Innovation and Technology Fund (projectITS/362/14FP) from the Innovation and Technology Commission, Grant Program of Sharif University of Technology (No. G930305) and the Elite National Institute.

Received: December 4, 2015
Revised: February 2, 2016
Published online: February 29, 2016

[1] S. D. Stranks, G. E. Eperon, G. Grancini, C. Menelaou, M. J. P. Alcocer, T. Leijtens, L. M. Herz, A. Petrozza, H. J. Snaith, *Science* **2013**, *342*, 341.
[2] T. Baikie, Y. Fang, J. M. Kadro, M. Schreyer, F. Wei, S. G. Mhaisalkar, M. Graetzel, T. J. White, *J. Mater. Chem. A* **2013**, *1*, 5628.
[3] S. Ahmad, G. V. Prakash, *J. Nanophotonics* **2014**, *8*, 083892.
[4] Q. Dong, Y. Fang, Y. Shao, P. Mulligan, J. Qiu, L. Cao, J. Huang, *Science* **2015**, *347*, 967.
[5] M. M. Lee, J. Teuscher, T. Miyasaka, T. N. Murakami, H. J. Snaith, *Science* **2012**, *338*, 643.
[6] M. Liu, M. B. Johnston, H. J. Snaith, *Nature* **2013**, *501*, 395.
[7] A. Kojima, K. Teshima, Y. Shirai, T. J. Miyasaka, *Am. Chem. Soc.* **2009**, *131*, 6050.
[8] H. Zhou, Q. Chen, G. Li, S. Luo, T.-B. Song, H.-S. Duan, Z. Hong, J. You, Y. Liu, Y. Yang, *Science* **2014**, *345*, 542.
[9] J. Burschka, N. Pellet, S.-J. Moon, R. Humphry-Baker, P. Gao, M. K. Nazeeruddin, M. Gratzel, *Nature* **2013**, *499*, 316.

[10] W. S. Yang, J. H. Noh, N. J. Jeon, Y. C. Kim, S. Ryu, J. Seo, S. I. Seok, *Science* **2015**, *348*, 1234.
[11] A. Kojima, K. Teshima, Y. Shirai, T. Miyasaka, *J. Am. Chem. Soc.* **2009**, *131*, 6050.
[12] G. E. Eperon, V. M. Burlakov, P. Docampo, A. Goriely, H. J. Snaith, *Adv. Funct. Mater.* **2014**, *24*, 151.
[13] H. Kim, H. Choi, J. Jeong, S. Kim, B. Walker, S. Song, J. Y. Kim, *Nanoscale* **2014**, *6*, 6679.
[14] Q. Chen, H. Zhou, Z. Hong, S. Luo, H. Duan, H. Wang, Y. Liu, G. Li, Y. Yang, *J. Am. Chem. Soc.* **2013**, *136*, 622.
[15] M. M. Tavakoli, Q. Lin, S. F. Leung, G. C. Lui, H. Lu, L. Li, B. Xiang, Z. Fan, *Nanoscale* **2016**, *8*, 4276.
[16] M. M. Tavakoli, L. Gu, Y. Gao, C. Reckmeier, J. He, A.L. Rogach, Y. Yao, Z. Fan, *Sci. Rep.* **2015**, *5*, 14083.
[17] M. M. Tavakoli, K.-H. Tsui, S.-F. Leung, Q. Zhang, J. He, Y. Yao, D. Li, Z. Fan, *ACS Nano* **2015**, *9*, 10287.
[18] Y. Cheng, Q.-D. Yang, J. Xiao, Q. Xue, H.-W. Li, Z. Guan, H.-L. Yip, S.-W. Tsang, *ACS Appl. Mater. Interfaces* **2015**, *7*, 19986.
[19] J. You, L. Meng, T.-B. Song, T.-F. Guo, Y. M. Yang, W.-H. Chang, Z. Hong, H. Chen, H. Zhou, Q. Chen, Y. Liu, N. D. Marco, Y. Yang, *Nat. Nanotechnol.* **2016**, *11*, 75.
[20] J.-Y. Jeng, K.-C. Chen, T.-Y. Chiang, P.-Y. Lin, T.-D. Tsai, Y.-C. Chang, T.-F. Guo, P. Chen, T.-C. Wen, Y.-J. Hsu, *Adv. Mater.* **2014**, *24*, 4107.
[21] A. S. Subbiah, A. Halder, S. Ghosh, N. Mahuli, G. Hodes, S. K. Sarkar, *J. Phys. Chem. Lett.* **2014**, *10*, 1748.
[22] Z. Zhu, X. Zheng, Y. Bai, T. Zhang, Z. Wang, S. Xiao, S. Yang, *Phys. Chem. Chem. Phys.* **2015**, *17*, 18265.
[23] D. Yang, R. Yang, J. Zhang, Z. Yang, S. F. Liu, C. Li, *Energy Environ. Sci.* **2015**, *8*, 3208.
[24] D. Liu, T. L. Kelly, *Nat. Photonics* **2014**, *8*, 133.
[25] D.-Y. Son, J.-H. Im, H.-S. Kim, N.-G. Park, *J. Phys. Chem. C* **2014**, *118*, 16567.
[26] M. H. Kumar, N. Yantara, S. Dharani, M. Graetzel, S. Mhaisalkar, P. P. Boix, N. Mathews, *Chem. Commun.* **2013**, *49*, 11089.
[27] Q. Hu, J. Wu, C. Jiang, T. Liu, X. Que, R. Zhu, Q. Gong, *ACS Nano* **2014**, *8*, 10161.
[28] J. Yang, B. D. Siempelkamp, E. Mosconi, F. D. Angelis, T. L. Kelly, *Chem. Mater.* **2015**, *27*, 4229.
[29] D. V. Talapin, J. S. Lee, M. V. Kovalenko, E. V. Shevchenko, *Chem. Rev.* **2009**, *110*, 389.
[30] M. M. Tavakoli, A. Simchi, H. Aashuri, *Mater. Chem. Phys.* **2015**, *156*, 163.
[31] A. Tayyebi, M. M. Tavakoli, M. Outokesh, A. Shafiekhani, A. Simchi, *Ind. Eng. Chem. Res.* **2015**, *54*, 7382.
[32] M. M. Tavakoli, H. Aashuri, A. Simchi, S. Kalytchuk, Z. Fan, *J. Phys. Chem. C* **2015**, *119*, 18886.
[33] M. M. Tavakoli, H. Aashuri, A. Simchi, Z. Fan, *Phys. Chem. Chem. Phys.* **2015**, *17*, 24412.
[34] M. M. Tavakoli, A. Tayyebi, A. Simchi, H. Aashuri, M. Outokesh, Z. Fan, *J. Nanopart. Res.* **2015**, *17*, 1
[35] M. M. Tavakoli, A. Simchi, Z. Fan, H. Aashuri, *Chem. Commun.* **2015**, *52*, 323.
[36] M. M. Tavakkoli, S. M. Abbasi, *Mater. Design* **2013**, *46*, 573.
[37] M. M. Tavakoli, R. Tavakoli, P. Davami, H. Aashuri, *J. Comput. Electron.* **2014**, *13*, 425.
[38] Y. Gao, H. Jin, Q. Lin, X. Li, M. M. Tavakoli, S. Leung, W. M. Tang, L. Zhou, H. L. Chan, Z. Fan, *J. Mater Chem. A* **2015**, *3*, 10199.
[39] J. T. W. Wang, J. M. Ball, E. M. Barea, A. Abate, J. A. Alexander-Webber, J. Huang, M. Saliba, I. Mora-Sero, J. Bisquert, H. J. Snaith, R. J. Nicholas, *Nano Lett.* **2013**, *14*, 724.
[40] D. I. Son, B. W. Kwon, J. D. Yang, D. H. Park, W. S. Seo, H. Lee, Y. Yi, C. L. Lee, W. K. Choi, *Nat. Nanotechnol.* **2012**, *7*, 465.